Ion-Selective Microporous Polymer Membranes with Hydrogen-Bond and Salt-Bridge Networks for Aqueous Organic Redox Flow Batteries

*Anqi Wang, Rui Tan, Dezhi Liu, Jiaxin Lu, Xiaochu Wei, Alberto Alvarez-Fernandez, Chunchun Ye, Charlotte Breakwell, Stefan Guldin, Anthony R. Kucernak, Kim E. Jelfs, Nigel P. Brandon, Neil B. McKeown, and Qilei Song**

Redox flow batteries (RFBs) have great potential for long-duration grid-scale energy storage. Ion-conducting membranes are a crucial component in RFBs, allowing charge-carrying ions to transport while preventing the cross-mixing of redox couples. Commercial Nafion membranes are widely used in RFBs, but their unsatisfactory ionic and molecular selectivity, as well as high costs, limit the performance and the widespread deployment of this technology. To extend the longevity and reduce the cost of RFB systems, inexpensive ion-selective membranes that concurrently deliver low ionic resistance and high selectivity toward redox-active species are highly desired. Here, high-performance RFB membranes are fabricated from blends of carboxylate- and amidoxime-functionalized polymers of intrinsic microporosity, which exploit the beneficial properties of both polymers. The enthalpy-driven formation of cohesive interchain interactions, including hydrogen bonds and salt bridges, facilitates the microscopic miscibility of the blends, while ionizable functional groups within the sub-nanometer pores allow optimization of membrane ion-transport functions. The resulting microporous membranes demonstrate fast cation conduction with low crossover of redox-active molecular species, enabling improved power ratings and reduced capacity fade in aqueous RFBs using anthraquinone and ferrocyanide as redox couples.

1. Introduction

Electrical energy storage constitutes an integral part of the large-scale deployment and integration of renewable but intermittent energy sources, such as wind and solar power.[1] Redox flow batteries (RFBs) are a promising grid-scale energy storage technology that offers a number of high-value opportunities for deep decarbonization due to their distinct features of high scalability, long discharge duration, decoupled energy storage and power generation, and inherently safe operation.[2] Conventional RFBs employ low-abundance metal-ion redox couples, such as vanadium, that are associated with technical challenges including relatively low energy density as well as high cost and environmental concerns, restricting their widespread commercial success.[2–4] Recently, organic and organometallic redox-active materials, such as quinone,[5] phenazine,[6] nitroxide radical,[7] viologen,[7,8] fluorenone,[9] organic iron complexes,[10,11] and their

A. Wang, R. Tan, D. Liu, J. Lu, X. Wei, Q. Song
Department of Chemical Engineering
Imperial College London
London SW7 2AZ, UK
E-mail: q.song@imperial.ac.uk
A. Alvarez-Fernandez, S. Guldin
Department of Chemical Engineering
University College London
London WC1E 7JE, UK

The ORCID identification number(s) for the author(s) of this article can be found under https://doi.org/10.1002/adma.202210098.

C. Ye, N. B. McKeown
EaStChem School of Chemistry
University of Edinburgh
Edinburgh EH9 3FJ, UK
C. Breakwell, A. R. Kucernak, K. E. Jelfs
Department of Chemistry
Molecular Sciences Research Hub
Imperial College London
London W12 0BZ, UK
N. P. Brandon
Department of Earth Science and Engineering
Imperial College London
London SW7 2AZ, UK

ADVANCED
SCIENCE NEWS

www.advancedsciencenews.com

ADVANCED
MATERIALS

www.advmat.de

modified analogs, have emerged as inexpensive and green alternatives to their inorganic counterparts for next-generation RFB development. Although these redox-active organic species offer structural diversity and tunability as well as potential cost-effectiveness, their chemical and electrochemical decomposition, which produces inactive species and leads to battery capacity fade, represents a major barrier to the commercialization of aqueous organic RFBs.[12] More recently, structural modifications of these molecular species have significantly improved their stability and facilitated the use of benign neutral-pH supporting electrolytes without the sacrifice of solubility, such as anthraquinone molecules functionalized with alkyl side chains terminated with carboxylate or phosphonate groups.[13–16] Nevertheless, chemical decomposition remains the dominant fade mechanism in many aqueous organic RFBs, even for some of the most stable chemistries. In addition, crossover of redox-active species through membrane separators is another mechanism for the capacity fade and unsatisfactory longevity of RFBs. Although a strategy of employing the same redox-active species in both catholyte and anolyte has been reported,[17,18] membrane crossover remains a common challenge for most RFB systems.

Ion-conducting membranes are a crucial component of RFBs and provide an electric-insulating barrier between the catholyte and anolyte while facilitating selective ion conduction to balance charge transfer during battery charging and discharging. Commercial Nafion membranes, which have demonstrated great success in fuel cell applications, are also widely employed in RFBs, but their nanoscale ion channels show poor selectivity toward redox-active molecular species dissolved in liquid electrolytes.[2,19] The high cost of Nafion and environmental concerns over its production are also factors that drive the development of alternative membrane materials. Hydrocarbon-based ion exchange membranes have been developed, following the same material design principle as Nafion—that is, introducing side chains bearing ion exchange groups to the hydrophobic macromolecular backbones to promote nanophase separation for the formation of water channels, but these membranes often require a much higher ion exchange capacity to achieve a comparable ionic conductivity to Nafion, leading to excessive swelling and poor selectivity.[20] Although inexpensive desalination and nanofiltration membranes made from nonionic polymers have demonstrated good performance in RFBs, the current efforts have been focused on acidic and alkaline systems such as vanadium flow battery and zinc–iron flow battery.[21]

More recently, polymers with sub-nanometer pores have emerged as membrane materials that can break the general permeability–selectivity trade-off for ion transport,[22] demonstrating promising performance in flow batteries[23,24] and lithium batteries.[25] In particular, polymers of intrinsic microporosity with amidoxime functional groups (AO-PIMs) have demonstrated remarkable ion-transport properties that combine low crossover of redox-active species with fast ion conduction, enabling improved cycling stability of alkaline flow batteries.[26,27] Nevertheless, the application of AO-PIMs is limited to alkaline systems only due to the high pK_a of AO groups ($pK_a = 13.2$) leading to a significant decrease in ionic conductivity at near-neutral pH. In recent work, the transport properties of AO-PIM membranes were optimized by tailoring polymer chain topology and pore architecture,[28] but their ionic conductivity remained low at near-neutral pH. This limitation necessitates the use of alternative ion exchange functionality ($pK_a < 7$) and new polymer design approaches for integration with the emerging neutral pH flow battery chemistries. Although there are good opportunities for the design of better membranes as the new redox chemistries do not require highly acidic or alkaline electrolytes, it remains challenging to design and synthesize cost-effective membranes that concurrently deliver low ionic resistance, high charge-carrier selectivity, and high stability.

Hydrogen-bond and salt-bridge interactions are ubiquitous in biological systems, the latter often arising from the charge–charge interactions between anionic carboxylate and cationic ammonium in amino acids of proteins. These cohesive interactions are particularly important in the stabilization of the entropically unfavorable folded structures of proteins as well as in the process of enzymatic catalysis.[29,30] Hydrogen bonding and salt bridges have been widely utilized in the design of synthetic supramolecular structures with applications ranging from ion binding to molecular recognition, sensing, and catalysis,[31,32] and enabled performance improvement of thin films and membranes for a variety of applications such as gas separation,[33,34] and electronic and optical devices.[35] Salt-bridge interactions, or more broadly, charge–charge interactions, have also been extensively employed for the fabrication of bipolar membranes and layer-by-layer assembly of nanofilms.[36] Although rarely explored in battery membrane separators,[37] these explicit interactions are attractive for the design and synthesis of hybrid membranes for ion conduction and could serve as interpolymer linkages to control membrane phase separation as well as the resulting nanostructures and ion-transport functions.

Here, we report a simple and effective strategy for preparing highly selective ion-conducting polymer membranes through the physical blending of carboxylate- and amidoxime-functionalized PIMs (cPIM-1 and AO-PIM-1, **Figure** 1a–c). High miscibility due to complementary hydrogen-bond and salt-bridge interactions eliminates the undesired phase separation and provides homogeneously distributed ion-transport pathways, in sharp contrast to a control sample based on the PIM-1|cPIM-1 blend membrane (Figure 1b–f). In these interpenetrating polymer blends, carboxylate groups along with amidoxime groups provide abundant ion-exchange sites for fast cation conduction, while the rigid polymer backbones limit swelling and electrolyte uptake to prevent the crossover of redox-active species. As a result, the resulting membranes show remarkable ion-transport performance and overcome the trade-off between ionic conductivity and selectivity. When integrated with an emerging anthraquinone|ferrocyanide flow battery chemistry, these microporous membranes demonstrate improved power rating and greatly reduced battery capacity fade as compared to commercial Nafion membranes and state-of-the-art AO-PIM membranes.

2. Results and Discussion

2.1. Highly Conductive Carboxylated PIM-1

Carboxylate groups were chosen to make highly conductive PIMs due to the ease of functionalization and lower hydration

2210098 (2 of 12)
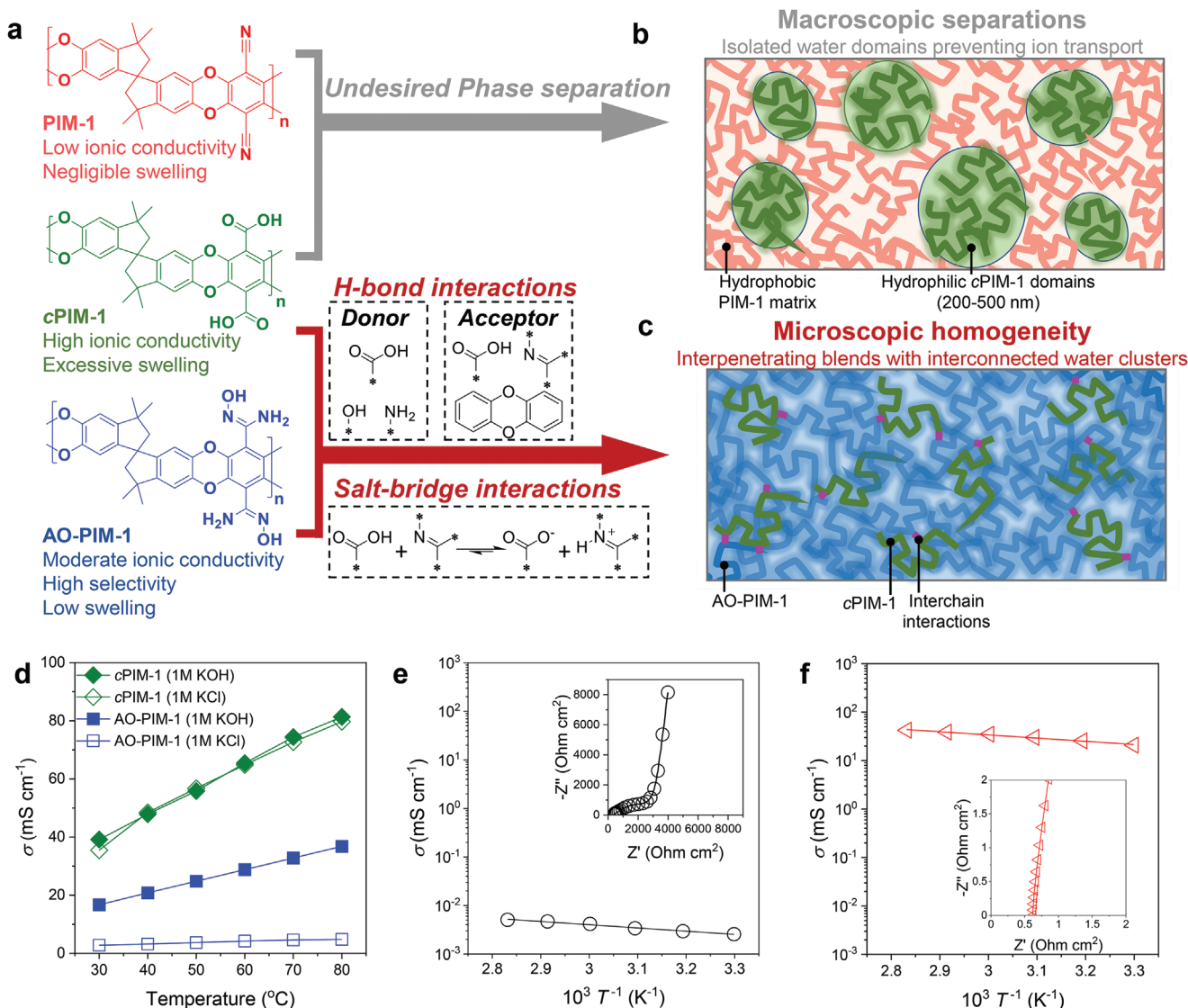
Figure 1. Membrane design. a) Chemical structures and key properties of PIM-1, cPIM-1, and AO-PIM-1. b,c) Schematic diagrams showing the morphology of blend membranes derived from cPIM-1 with PIM-1 (b) or AO-PIM-1 (c). d) Apparent ionic conductivity of cPIM-1 and AO-PIM-1. e,f) Temperature-dependent ionic conductivity of blend membranes, PIM-1|cPIM-1 blend (e) and AO-PIM-1|cPIM-1 blend (f) measured from 1 M aqueous KOH. Inset figures are electrochemical impedance spectra at 30 °C. cPIM-1 blending ratio is 20 wt%.

levels as compared to the other low-pK_a ion exchange chemistries (e.g., sulfonate).[38] Carboxylated PIM-1 (cPIM-1) was prepared by facile acid hydrolysis. Nuclear magnetic resonance (NMR) spectra is shown in Figure S1 in the Supporting Information.[39] Measurement of intrinsic viscosity confirmed the comparable molecular weight of cPIM-1 and PIM-1 (0.30 and 0.26 dL g^{-1}, respectively), while the molecular weight of the latter was analyzed by gel permeation chromatography giving a M_w of 128 000 g mol^{-1} and a polydispersity index (PDI) of 2.53. Some microporosity was found to be retained in cPIM-1 after the modification but with a reduced apparent Brunauer–Emmett–Teller surface area of 318 m^2 g^{-1}, in contrast to 778 m^2 g^{-1} for PIM-1,[26] as calculated from nitrogen sorption isotherms (**Figure 2**a). This can be attributed to strong hydrogen-bond interactions induced by carboxylic acid groups that lead to a denser packing of polymer chains. The high carbon dioxide

adsorption capacity of cPIM-1 (Figure 2b), especially in the low-pressure range, indicated a greater portion of accessible pores in the ultra-microporous range (<0.7 nm, Figure 2c). Wide-angle X-ray scattering (WAXS) and small-angle X-ray scattering (SAXS) measurements were performed to evaluate the microstructure of cPIM-1. The characteristic peaks in WAXS for cPIM-1 were found in similar positions to those of PIM-1 and AO-PIM-1 at around 0.95, 1.24, and 1.62 Å^{-1} (Figure 2d,f), suggesting a matching intersegmental spacing and chain packing among these polymers. When fully hydrated and exchanged with potassium ions, cPIM-1 membrane exhibited a new peak at q position of 1.5 Å^{-1} (≈0.42 nm in real space, Figure 2e,g), which may relate to the water clusters formed within their sub-nanometer pores. In contrast to the ionomer peaks of Nafion membranes at q ≈ 0.15 Å^{-1} (4.2 nm in real space) that arise from correlation spacing between the hydrophilic sulfonate-rich
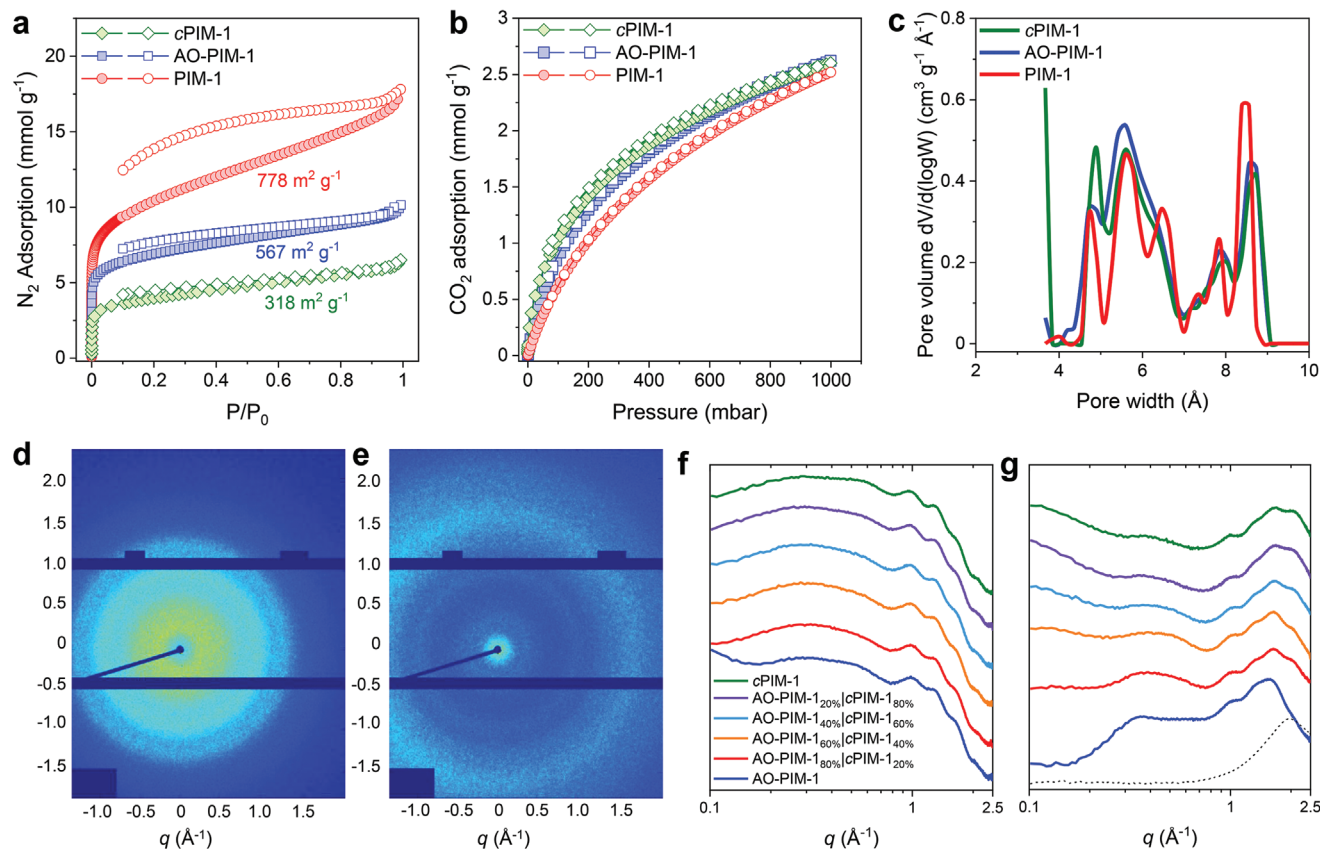
Figure 2. Porosity characterization. a) N_2 sorption isotherm at 77K. b) CO_2 sorption isotherm at 273K. c) Pore size distribution derived from CO_2 sorption isotherm based on density-functional theory (DFT) calculations. Data for PIM-1 and AO-PIM-1 are digitalized from ref. [26]. d,e) WAXS 2D scattering patterns of cPIM-1 membrane in the dry state (d) and fully hydrated state (e). f,g) WAXS 1D plots of cPIM-1, AO-PIM-1, and their blends in the dry (f) and fully hydrated state (g). Fully hydrated membranes were prepared by soaking in 1 м aqueous KCl solution. Dashed line in (g) corresponds to the spectrum of 1 м aqueous KCl.

domains,[28] the SAXS spectrum of cPIM-1 did not show any significant scattering features over a wide low-q range of 0.05–0.3 Å^{-1} (Figure S2, Supporting Information). These results highlight the unique mechanism for the formation of water channels in PIM-based ion exchange membranes: the high rigidity of the polymer chain poses a significant barrier to the self-assembly of chain segments toward nanophase separation, while percolation of their intrinsic sub-nanometer pores generates well-defined pathways where ion exchange sites are uniformly distributed for fast and selective ion transport.

A potassium-ion-exchanged cPIM-1 membrane showed ultrahigh apparent ionic conductivity values of 39–81 mS cm^{-1} over a temperature range of 30–80 °C in 1 м KCl aqueous solution, as measured by electrochemical impedance spectroscopy (EIS). These values are comparable to those measured in alkaline solutions (1 м KOH) for the same membrane and exceed those previously reported for microporous ion-transport membranes (Figure 1d).[23,26–28,40] By contrast, apparent ionic conductivity of AO-PIM-1 membranes measured in neutral pH electrolytes was significantly lower than that in alkaline electrolytes (Figure 1d). The superior ionic conductivity of cPIM-1 is attributed to its low pK_a (pK_a = 3.5 and 4.8) that avoids the reprotonation of carboxylate over a wider pH range, as well as a high theoretical ion exchange capacity (IEC) value of 4.0 mEq g^{-1}. However,

the high IEC, which exceeds the typical values for practical cation exchange membranes (0.8–2 mEq g^{-1}), leads to excessive swelling and the loss of membrane robustness. Although potassium-ion-exchanged cPIM-1 remained intact in 1 м electrolyte solutions, allowing for conductivity measurements, the membrane quickly dissolved in deionized water at ambient conditions (Figure S3, Supporting Information). This interesting behavior is in good agreement with the well-known polyelectrolyte phenomena: continuous adsorption of water into the polymer matrix is driven by the osmotic forces from the mobile potassium ions dissociated from the polymer as well as the electrostatic repulsion between polymer negative charges, leading to the full dissolution of polymers, while these forces are effectively shielded in high concentration supporting electrolytes (e.g., 1 м KOH and KCl).

Despite the ultrafast ion conduction in cPIM-1, its potential use as a membrane separator in electrochemical devices is prohibited by excessive swelling and mechanical fragility. Hence, it is important to regulate the overall IEC of membranes derived from cPIM-1. One potential approach is to achieve partial hydrolysis through optimizing reaction conditions or controlling the stoichiometric ratios of reagents used. However, the multistep reaction mechanism for the benzonitrile-to-carboxylate conversion involves the formation of a stable amide
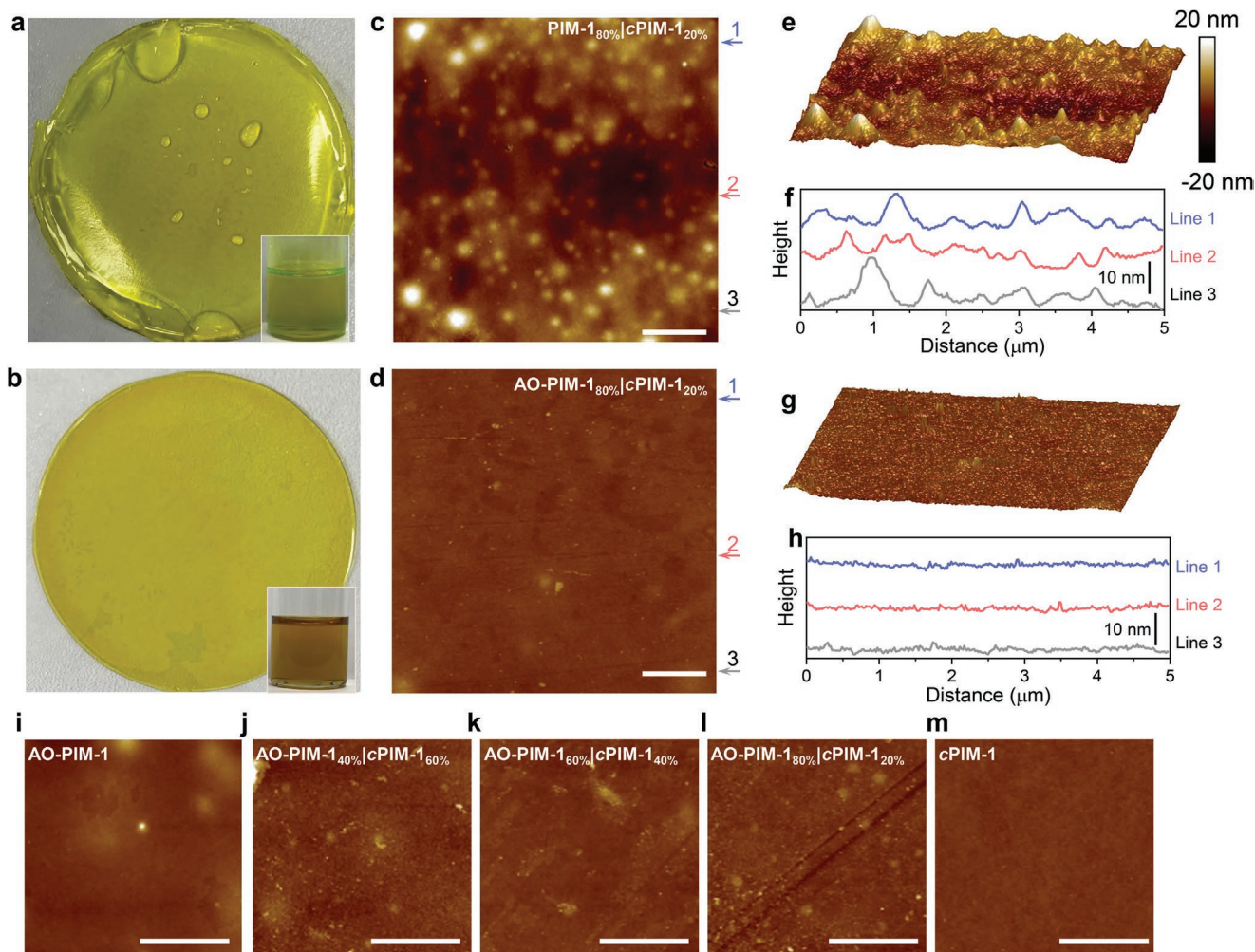
Figure 3. Characterization of phase separation. a,b) Photos of PIM-1|*c*PIM-1 blend (a) and AO-PIM-1|*c*PIM-1 blend (b) membranes. *c*PIM-1 blending ratio is 20 wt%. Inset figures are photos of blend polymer solutions. c–h) 2D and 3D AFM images and height profiles of PIM-1|*c*PIM-1 blend (c,e,f) and AO-PIM-1|*c*PIM-1 blend (d,g,h) membranes. i–m) AFM images of AO-PIM-1|*c*PIM-1 blend membranes. Scale bar: 1 µm.

intermediate, resulting in a complex mixture of amide, carboxylic acid, and unreacted nitrile groups with uncontrollable ratios when performing partial hydrolysis.[41–43] Alternatively, physical blending with another polymer may allow the properties of *c*PIM-1 to be optimized for ionic conduction, swelling, and mechanical robustness. In particular, carboxylic acid groups in *c*PIM-1 are capable of ionic interactions and acting as both H-bond acceptors and donors, providing opportunities to control the morphology of the blend membranes through tailoring interpolymer interactions.

2.2. Choice of Polymer for Physical Blending with *c*PIM-1

In the design of miscible polymer blends, thermodynamics favors a low enthalpy of mixing that contributes to a negative value of Gibbs free energy of mixing. The enthalpy of mixing can be manipulated by controlling both the chain structure and the specific interactions between complementary functional groups of the two polymers.[44] PIM-1 and AO-PIM-1 were

used to prepare blends with *c*PIM-1. Both polymers have the same chain structure of high rigidity as that of *c*PIM-1, while the nitrile in PIM-1 and amidoxime in AO-PIM-1 enable variation in interpolymer interactions with *c*PIM-1. Tetrahydrofuran (THF) and *N*-methyl-2-pyrrolidone (NMP) were used as the solvent for blending *c*PIM-1 with PIM-1 and AO-PIM-1, respectively, forming homogeneous and transparent solutions and visibly homogeneous membranes after solvent evaporation (**Figure 3**a,b). A blending ratio of 20 wt% for *c*PIM-1 was employed to give an estimated overall membrane IEC value of ≈0.8 mEq g^{-1} based on the content of carboxylates, a value comparable to that of Nafion membranes. Ionic conductivity of the AO-PIM-1|*c*PIM-1 blend membrane was 21 mS cm^{-1} in 1 M aqueous KOH solution at 30 °C (Figure 1f), approximately half that of *c*PIM-1, while the blend membrane based on PIM-1 showed ionic conductivity as low as 0.0026 mS cm^{-1} under the same testing conditions (Figure 1e). The large disparity in ionic conductivity suggests a fundamentally different structure and morphology in the blend membranes for PIM-1|*c*PIM-1 and AO-PIM-1|*c*PIM-1.
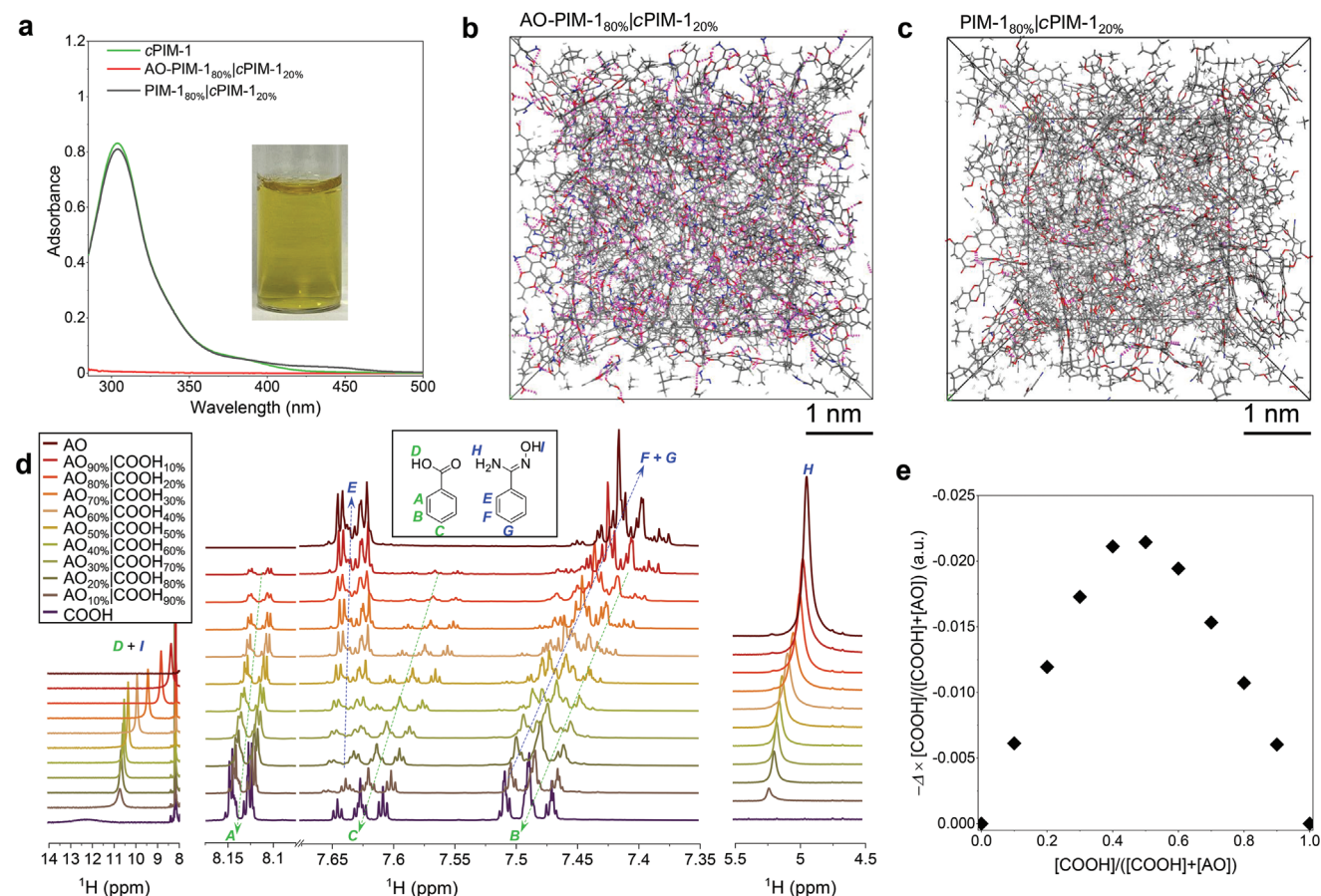
Figure 4. Characterization of interpolymer interactions. a) UV–vis spectra of the washing solution. Inset shows aqueous solution of potassium-exchanged cPIM-1 (0.075 mg mL^{-1}). b,c) 3D view of amorphous cells of AO-PIM-1$_{80\%}$|cPIM-1$_{20\%}$ (b) and PIM-1$_{80\%}$|cPIM-1$_{20\%}$ (c) blends. The cells consist of 4 cPIM-1 polymer chains and 16 AO-PIM-1/PIM-1 polymer chains, each containing 10 repeat units. Cell size in (b): $54 \times 54 \times 54$ Å^3; cell size in (c): $53 \times 53 \times 53$ Å^3. The purple dashed lines in (b) and (c) represent hydrogen bonds. d) Partial ^{1}H NMR spectra of model compound blends in d-chloroform with a total concentration of 10 mmol L^{-1} as a function of blending ratio. e) Job's plot for proton C in benzoic acid.

To understand the structural features that lead to the different ionic conductivities of the blend membranes, potential phase separation was investigated using atomic force microscopy (AFM), solubility tests, and scanning electron microscopy with energy-dispersive X-ray analysis (SEM–EDX). AFM images in Figure 3c–f show a phase-separated morphology in the PIM-1|cPIM-1 blend membrane with scattered nodules randomly distributed within a matrix of the other polymer phase. These nodules, likely the cPIM-1-rich domains, vary in the range of ≈200–500 nm in size and ≈5–15 nm in height (Figure 3f). By contrast, the surface of the AO-PIM-1|cPIM-1 blend membrane is flat and featureless (Figure 3d,g,h and Figure S4 (Supporting Information)), indicating a higher degree of nanoscale miscibility of the binary polymer phases. To understand how polymer chains mix within the blend, we examined PIM-1|cPIM-1 and AO-PIM-1|cPIM-1 membrane solubility in deionized water noting the complete dissolution of cPIM-1 in deionized water after potassium exchange (**Figure 4**a). For the PIM-1|cPIM-1 membrane that was soaked in distilled water after potassium-ion exchange, the resulting yellow solution gave a peak of comparable intensity in the UV–vis spectrum to that of the cPIM-1 membrane, suggesting the full dissolu-

tion of the cPIM-1 phase. SEM–EDX further confirmed that no potassium could be detected for the treated PIM-1|cPIM-1 blend membrane (Figures S5 and S6, Supporting Information). By contrast, the colorless solution obtained from the AO-PIM-1|cPIM-1 blend membrane indicated the stabilization of the cPIM-1 phase within the blend. The change of solubility for cPIM-1 is related to the degree of phase separation, as the high miscibility between cPIM-1 and AO-PIM-1 provides sufficient chain entanglement and mechanical confinement that prevents cPIM-1 from dissolution.

The high miscibility of AO-PIM-1 and cPIM-1 is attributed to their abundant interchain interactions. A high density of H-donating OH and NH$_2$ motifs in the amidoxime groups form hydrogen-bonding interactions with the carbonyl in carboxylic acid groups, while a pK_a window between carboxylic acid and amidoxime promotes a spontaneous acid–base reaction,[45] generating salt-bridge interactions. Although the dioxin and benzonitrile segments in PIM-1 are potential H-bond acceptors, the interpolymer interactions with cPIM-1 appeared insufficient to eliminate phase separation. Molecular simulations confirmed the formation of an extensive network of hydrogen bonds in the AO-PIM-1|cPIM-1 blend in sharp contrast to PIM-1|cPIM-1

**ADVANCED
SCIENCE NEWS**

www.advancedsciencenews.com

**ADVANCED
MATERIALS**

www.advmat.de

blend (Figure 4b,c and Figure S7 (Supporting Information)). NMR measurements further provided a molecular-level understanding of interpolymer interactions within the blends. Figure 4d presents the ^{1}H NMR spectra of the blends for model compounds (i.e., benzamidoxime and benzoic acid) as a function of the blending ratio. On increasing the ratio of benzamidoxime, the proton signals corresponding to the amine motif in AO groups appear and move toward lower chemical shifts with the peak intensity building up proportionally, while carboxylic acid resonance changes from a broad peak to a narrow one and shifts upfield. Integration of the resonance shifting in the range of 11–8 ppm was found independent of the blending ratio when the benzamidoxime portion was greater than 20%, and was equivalent to the sum of hydroxyl in AO groups and carboxylic acid, suggesting their fast proton exchange due to intermolecular association. Noticeable peak shift was also found for aromatic protons providing further evidence for the strong interactions between the two species. A Job's plot for proton C in benzoic acid indicated a 1:1 complexation stoichiometry between amidoxime and carboxylic acid model compounds likely through a combination of hydrogen-bonding and salt-bridge formation.

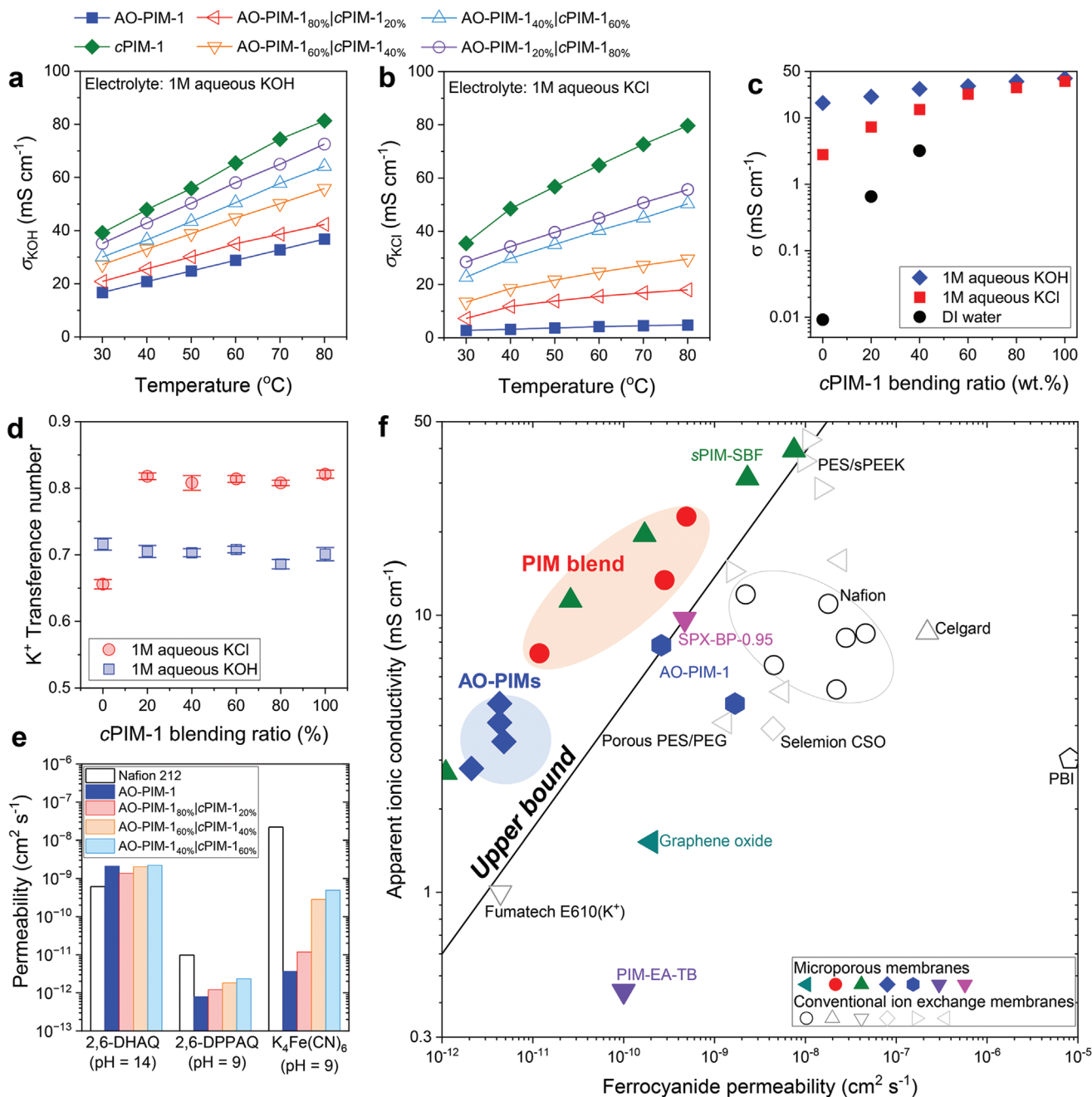### 2.3. Ionic and Molecular Transport in AO-PIM-1|cPIM-1 Membranes

To optimize ion-transport functions, further films of AO-PIM-1|cPIM-1 containing 20–80 wt% cPIM-1 (e.g., denoted as AO-PIM-1$_{20\%}$|cPIM-1$_{80\%}$) were fabricated with the composition confirmed by Fourier transform infrared spectroscopy (FT-IR) (Figure S8, Supporting Information). Topographical AFM images in Figure S4 (Supporting Information) show flat and featureless surfaces for all the membranes, suggesting miscibility at all proportions. Solubility test in deionized water confirmed strong interpenetration between the two polymer components in the blend as cPIM-1 was found to be completely retained when its content was below 80% (Figure S9, Supporting Information). Of note, all membranes including cPIM-1 membrane were insoluble in 1 M aqueous KOH and KCl. Tensile tests indicated excellent mechanical properties with ultimate tensile strength ranging from 65 to 90 MPa (Figure S10, Supporting Information).

Apparent ionic conductivity of the blend membranes measured in 1 M aqueous KOH (σ_{KOH}) increased linearly from 21 mS cm^{-1} for AO-PIM-1$_{80\%}$|cPIM-1$_{20\%}$ to 39 mS cm^{-1} for AO-PIM-1$_{20\%}$|cPIM-1$_{80\%}$ at 30 °C (**Figure** 5a), accompanied by an increase in membrane electrolyte uptake and swelling ratio (Figure S11, Supporting Information). A similar trend was observed for apparent ionic conductivity measured in 1 M aqueous KCl (σ_{KCl}), with a steady increase of $\sigma_{KCl}/\sigma_{KOH}$ ratio from 35% for AO-PIM-1$_{80\%}$|cPIM-1$_{20\%}$ to 81% for AO-PIM-1$_{20\%}$|cPIM-1$_{80\%}$ (Figure 5b,c). Generally, ion-transport membranes show a slightly lower apparent ionic conductivity in aqueous solutions of KCl than in that of KOH ($\sigma_{KCl}/\sigma_{KOH} < 100\%$) due to the difference in ionic mobility of Cl$^-$ and OH$^-$ that are absorbed within ion-transport channels, especially for microporous membranes where selectivity of ion transport is mainly size-based. However, for cation exchange membranes, the presence of a high density of negative charges excludes mobile anions more effectively (i.e., Donnan exclusion), resulting in ion conduction being dominated by cations and the value of $\sigma_{KCl}/\sigma_{KOH}$ approaching unity. The high value of $\sigma_{KCl}/\sigma_{KOH}$ for AO-PIM-1|cPIM-1 membranes at high cPIM-1 content suggests the role of the Donnan effect as a significant mechanism governing the ion-conduction processes. Ion transference number was further measured to quantify the relative contribution of cations and anions to the apparent ionic conductivity (Figure 5d). AO-PIM-1, cPIM-1, and their blends showed a comparable potassium-ion transference number in alkaline supporting electrolyte (0.701 ± 0.010 for cPIM-1), suggesting the similar charge environment within these membranes. However, the value for a charge-neutral AO-PIM-1 decreased to only 0.544 ± 0.011 in 1 M aqueous KCl, and pretreatment at high pH for deprotonation of AO groups only improved the value to 0.656 ± 0.007 (the influence of pretreatment has been discussed in our previous work[26]); by contrast, a higher potassium-ion transference number ($\approx$0.81) was achieved for cPIM-1 and blend membranes. The lower potassium-ion transference number in AO-PIM-1 at neutral pH is attributed to the weak Donnan effect, as the majority of amidoxime groups become charge-neutral, whereas the introduction of heavily charged cPIM-1 in the blend membranes significantly enhances Donnan exclusion to selectively conduct cations.

To further investigate cation conductivity, intrinsic ionic conductivity ($\sigma_{intrinsic}$) was measured in deionized water, where ion conduction relies only on the mobile potassium ions dissociated from polymer chains (Figure S12, Supporting Information). Ionic conductivity of potassium-exchanged AO-PIM-1 decreased substantially to only 0.0092 mS cm^{-1} in deionized water, a value roughly 0.3% of that of σ_{KCl}, indicating that ion transport in AO-PIM-1 is dominated by the electrolyte ions absorbed in the micropores (Figure S13, Supporting Information). This mechanism is in good agreement with the high pK_a value of AO groups and is also supported by the low $\sigma_{KCl}/\sigma_{KOH}$ value of AO-PIM-1 (17%). Despite the solubility of cPIM-1 in water following exchange with potassium cations, membranes of AO-PIM-1$_{80\%}$|cPIM-1$_{20\%}$ and AO-PIM-1$_{60\%}$|cPIM-1$_{40\%}$ both remained intact following this treatment, allowing their intrinsic ionic conductivity values of 0.654 and 3.2 mS cm^{-1} to be measured, corresponding to 9% and 24% of their apparent ionic conductivity, respectively (Figure 5c and Figure S13 (Supporting Information)). However, AO-PIM-1$_{40\%}$|cPIM-1$_{60\%}$ and AO-PIM-1$_{20\%}$|cPIM-1$_{80\%}$ membranes became too brittle to handle for tests in deionized water, hence their intrinsic conductivity was not measured.

Selective ion transport of AO-PIM-1|cPIM-1 membranes was demonstrated by diffusion dialysis tests using potassium ferrocyanide, the catholyte material of choice used in most aqueous organic RFBs (Figure 5e and Figure S14 and Tables S1 and S2 (Supporting Information)). In previous studies,[26,28] we have demonstrated the lower ferrocyanide permeability of AO-PIM-1 than that of Nafion 212 (1.7 × 10^{-9} and 2.8 × 10^{-8} cm^2 s^{-1}, respectively) at pH = 14, resulting from the higher size-based selectivity of the former. By reducing electrolyte pH from 14 to 9, ferrocyanide permeability for AO-PIM-1 was further reduced to 3.6 × 10^{-12} cm^2 s^{-1}, while Nafion 212 showed comparable ferrocyanide permeability in both near neutral-pH

**ADVANCED
SCIENCE NEWS**

www.advancedsciencenews.com

**ADVANCED
MATERIALS**

www.advmat.de

Figure 5. Selective ionic and molecular transport. a,b) Apparent ionic conductivity of blend membranes measured in 1 M aqueous KOH (a) and 1 M aqueous KCl (b). c) Ionic conductivity as a function of cPIM-1 content. d) Potassium ion transference number as a function of cPIM-1 content measured in 1 M aqueous KOH and KCl. e) Permeability of 2,6-DHAQ, 2,6-DPPAQ, and potassium ferrocyanide. f) Upper bound plot showing the trade-off between ionic conductivity and selectivity. Data presented in this figure are listed in Table S2 (Supporting Information). The line represents an empirical upper bound for the trade-off between ionic conductivity and permeability of redox-active species for RFB membranes.

and alkaline conditions (2.2 × 10^{-8} cm^2 s^{-1} at pH 9).[28] The greatly enhanced selectivity of AO-PIM-1 is associated with its lower electrolyte uptake and swelling when electrolyte pH is lower than the pK_a (13.4) of AO groups (Figure S11, Supporting Information). The reduced electrolyte uptake in AO-PIM-1 limits the size of water clusters that facilitate ion transport and provides higher size-sieving selectivity, whereas ionic conduc-

tivity of AO-PIM-1 is compromised. By contrast, the electrolyte uptake and swelling ratio of cPIM-1 were found independent of electrolyte pH (Figure S11, Supporting Information) due to the deprotonation of carboxylate groups and the dissociation of their counterions across the neutral and alkaline pH regions. On increasing the cPIM-1 blending ratio, the ferrocyanide permeability gradually increased to values up to 4.9 × 10^{-10} cm^2 s^{-1}

**ADVANCED
SCIENCE NEWS**

www.advancedsciencenews.com

**ADVANCED
MATERIALS**

www.advmat.de

for AO-PIM-1$_{40\%}$|cPIM-1$_{60\%}$, due to swelling forming less size-selective pathways for transport of large ions. Nevertheless, all AO-PIM-1|cPIM-1 membranes show significantly lower crossover of redox-active species relative to Nafion membranes. Indeed, ferrocyanide permeability for AO-PIM-1|cPIM-1 membranes are up to two orders of magnitude lower than that of Nafion 212 membranes, while ionic conductivity is comparable to commercial Nafion membranes. Importantly, AO-PIM-1|cPIM-1 shows improvement in ion-transport performance with data points of permeability versus conductivity above the performance upper bound of previously reported RFB membranes (Figure 5f).

We further evaluated the selectivity of AO-PIM-1|cPIM-1 membranes toward redox-active molecular species that are used as high-performance anolyte materials in aqueous organic RFBs (Figure 5e and Figure S14 and Table S1 (Supporting Information)), including 2,6-dihydroxyanthraquinone (2,6-DHAQ)[5] and 2,6-di(3-phosphenopropoxy)anthraquinone (2,6-DPPAQ).[15] For each film, the permeability of 2,6-DHAQ at pH 14 was comparable to that for AO-PIM-1 with values in the order of 10^{-9} cm^2 s^{-1}, suggesting the retention of molecular selectivity in cPIM-1-rich membranes. However, these values are unfavorably higher in comparison with those of Nafion and Fumasep E600 membranes.[16] Of note, 2,6-DHAQ permeability for Nafion in the literature varies in the range of 10^{-11} to 10^{-9} cm^2 s^{-1} likely due to different protocols being followed for membrane pre-treatment (Table S2, Supporting Information),[16,23,26,28] which have a profound influence on Nafion morphology and ion-transport functions.[19] We attribute the moderate 2,6-DHAQ selectivity of PIM-based microporous membranes to the small molecular size of 2,6-DHAQ (molecular weight of 240 g mol^{-1}) and the cohesive π–π interactions between this aromatic compound with PIMs, which are composed of fused-benzene rings in macromolecular structures, as suggested by the strong adsorption of 2,6-DHAQ in PIM membranes.[28] For the charge-reinforced, bulkier 2,6-DPPAQ (four negative charges per molecule and molecular weight of 484 g mol^{-1}), permeability values decreased significantly to 7.9×10^{-13} cm^2 s^{-1} for AO-PIM-1 and 1.2–2.3×10^{-12} cm^2 s^{-1} for AO-PIM-1|cPIM-1 at pH 9, several times lower than that of Nafion 212. The higher charge density in 2,6-DPPAQ may enhance Donnan exclusion from the negatively charged polymer functionalities, while its alkyl side chains and larger molecular size likely reduce the undesired adsorption within PIM membrane micropores.
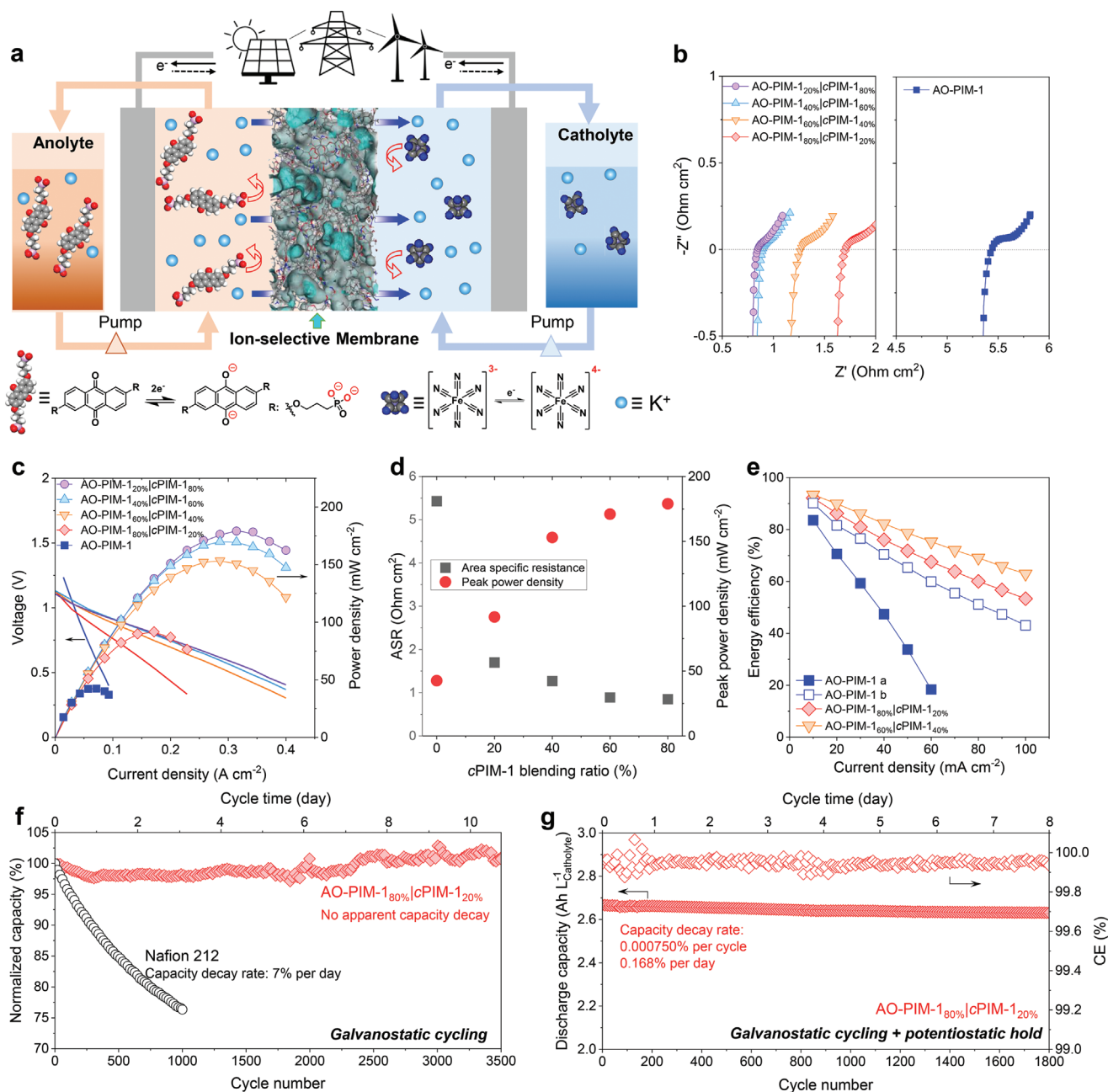
2.4. Redox Flow Battery Performance

Laboratory-scale RFB cells were assembled by pairing the AO-PIM-1|cPIM-1 membranes with 2,6-DPPAQ|K$_4$Fe(CN)$_6$ redox couple at pH 9 (**Figure 6**a). This particular redox couple was selected due to their proven chemical and electrochemical stability at (near-)neutral pH among a variety of flow battery chemistries.[12,15] Different from the original report of 2,6-DPPAQ,[15] where 2,6-DPPAQ was used as the capacity-limiting side, we chose ferrocyanide as the capacity-limiting electrolyte in this work due to the considerations that the capacity decay in the former condition is dominated by 2,6-DPPAQ degradation instead of membrane crossover and that ferrocyanide does not

show any degradation at neutral pH,[11,46,47] enabling us to focus on the evaluation of membrane crossover during cell operation.

RFBs based on AO-PIM-1|cPIM-1 blend membranes displayed low high-frequency area-specific resistance (ASR$_{hf}$) with values ranging from 1.70 Ω cm^2 for AO-PIM-1$_{80\%}$|cPIM-1$_{20\%}$ to 0.85 Ω cm^2 for AO-PIM-1$_{20\%}$|cPIM-1$_{80\%}$ (Figure 6b), while an otherwise identical RFB with an AO-PIM-1 membrane showed an ASR$_{hf}$ of 5.43 Ω cm^2. The peak power density increased linearly as a function of cPIM-1 proportion in the blend membranes from 43 mW cm^{-2} for AO-PIM-1 to 179 mW cm^{-2} for AO-PIM-1$_{20\%}$|cPIM-1$_{80\%}$ (Figure 6c,d, Table S3 (Supporting Information). At current densities higher than 60 mA cm^{-2}, the RFB based on the AO-PIM-1 membrane could not perform charge–discharge cycles; reducing membrane thickness from 90 to 47 μm led to a lower ASR$_{hf}$ of 2.73 Ω cm^2 and an improvement of energy efficiency from 18% to 60% at a current density of 60 mA cm^{-2} (Figure 6e and Figure S15 (Supporting Information)). By contrast, flow cells assembled with low-resistance PIM-1|cPIM-1 membranes exhibited greatly enhanced energy efficiencies of 68% for AO-PIM-1$_{80\%}$|cPIM-1$_{20\%}$, and 75% for AO-PIM-1$_{60\%}$|cPIM-1$_{40\%}$.

Long-term RFB cycling test was further performed with a focus on AO-PIM-1$_{80\%}$|cPIM-1$_{20\%}$ membrane due to its low ionic resistance and low redox-species crossover rate combined with excellent mechanical robustness. Fluctuations and a slight increase in discharge capacity was observed for a RFB assembled with AO-PIM-1$_{80\%}$|cPIM-1$_{20\%}$ membrane during the purely galvanostatic cycling of 3500 cycles over 257 h at 80 mA cm^{-2} (Figure 5f). This phenomenon has been observed previously[18] as is related to the inherent limitation of galvanostatic cycling, which accesses only part of the total capacity and is sensitive to drifts of internal cell resistance.[13] In contrast to the zero loss of apparent capacity, an otherwise-identical RFB assembled with Nafion 212 membrane lost 23.6% of its initial capacity over 1000 galvanostatic cycles of charging and discharging at 80 mA cm^{-2}, equivalent to a demonstrated capacity fade of 0.0236% per cycle and 7% per day (cycling result of Nafion 212 was initially reported in our previous work[28]). Cycled electrolytes of both RFBs were qualitatively analyzed by cyclic voltammetry to evaluate the crossover of redox-active species. 2,6-DPPAQ was not detected in the cycled catholytes of both RFBs, while a small peak corresponding to ferrocyanide was found in the cycled anolyte of the RFB assembled with AO-PIM-1$_{80\%}$|cPIM-1$_{20\%}$ and a significantly larger ferrocyanide peak for that of RFB assembled with Nafion 212 (Figure S16, Supporting Information). In addition, quantitative analysis of the anolyte composition using inductively coupled plasma mass spectrometry gave a ferrocyanide crossover rate of 0.00037% per cycle (0.12% per day) for the RFB assembled with AO-PIM-1$_{80\%}$|cPIM-1$_{20\%}$, which provides an estimate of the actual capacity loss rate in the cell. To exclude the artefacts induced by temporal variations in accessible capacity during purely galvanostatic cycling, a potentiostatic hold was added at the end of each galvanostatic half-cycle at 80 mA cm^{-2} until the current density fell below 2 mA cm^{-2}, a testing protocol widely used for the evaluation of RFB systems with medium and low capacity fade at 100% state of charge.[12,13] Under this testing condition, full capacity (>99.5%) was accessed in a RFB assembled with AO-PIM-1$_{80\%}$|cPIM-1$_{20\%}$ membrane during the initial cycles

Figure 6. 2,6-DPPAQ|K$_4$Fe(CN)$_6$ redox flow battery performance. a) Schematic diagram showing a RFB assembled with ion-selective membranes. b) EIS spectra of flow cells assembled with AO-PIM-1 and blend membranes at 100% state of charge (SOC). c) Voltage and power density versus current density at ≈100% SOC. d) Area-specific resistance (ASR) and peak power density as a function of cPIM-1 blending ratio. e) Energy efficiency as a function of current density. Membrane thickness: 90 μm (AO-PIM-1-a), 47 μm (AO-PIM-1-b), 58 μm (AO-PIM-1$_{80\%}$|cPIM-1$_{20\%}$), 104 μm (AO-PIM-1$_{60\%}$|cPIM-1$_{40\%}$), 127 μm (AO-PIM-1$_{40\%}$|cPIM-1$_{60\%}$), and 151 μm (AO-PIM-1$_{20\%}$|cPIM-1$_{80\%}$). AO-PIM-1-a was used in (a) and (b). f) Stability of galvanostatic cycling for RFBs assembled with AO-PIM-1$_{80\%}$|cPIM-1$_{20\%}$ membrane (67 μm) and Nafion 212 at 80 mA cm^{-2}. Capacity was normalized based on the discharge capacity of the first cycle. Cycle time is based on the RFB assembled with the AO-PIM-1$_{80\%}$|cPIM-1$_{20\%}$ membrane. Cycling data for Nafion 212 under the same operating conditions were replotted from ref. [28]. g) Coulombic efficiency (CE) and cycling stability of a RFB assembled with AO-PIM-1$_{80\%}$|cPIM-1$_{20\%}$ membrane (50 μm); this cell was cycled galvanostatically at 80 mA cm^{-2} with each half-cycle ended with a potentiostatic hold until the current density fell below 2 mA cm^{-2}. Anolyte: 0.1 M 2,6-DPPAQ in 1 M KCl at pH 9 (10 mL); catholyte: 0.1 M K$_4$Fe(CN)$_6$ in 1 M KCl at pH 9 (10 mL), affording a theoretical capacity of 2.68 Ah L$_{catholyte}$$^{-1}$. The catholyte was the capacity-limiting side with an electron ratio of 1:2 between catholyte and anolyte. The data are shown in every 20 cycles in (f) and every 10 cycles in (g).

followed by a steady capacity decay rate of 0.000750% per cycle (0.168% per day) in 1800 charge–discharge cycles over 192 h. This demonstrated decay rate is slightly higher than the "esti-

mated" decay rate for the galvanostatically cycled cell (0.12% per day) due to the difference in membrane thickness (69 μm for the galvanostatic cycling and 50 μm for the galvanostatic

cycling followed by potentiostatic hold). This low value of performance decay obtained from an operating cell is comparable to those from RFBs assembled with topologically optimized AO-PIMs (0.13–0.16% per day)[28] and superior to catholyte-limiting RFBs based on commercial membranes (Table S4, Supporting Information).

3. Conclusion

We report a series of microporous polymer membranes that combine fast cation conduction with high size-sieving selectivity and demonstrate their promising performance as ion-selective membranes for long-cycling aqueous organic RFBs. The key design principle of these blend membranes is the control over polymer functionality to prevent phase separation and enable good miscibility by leveraging hydrogen- and salt-bridge interpolymer interactions. These allow the formation of continuously interconnected water clusters across multiple polymer phases for efficient ion conduction, while the rigid microporous structure ensures high selectivity toward small redox-active species. Over the past two decades, innovations in materials chemistry have enabled many membrane-based technologies to mature for practical uses, from molecular separation processes, such as gas separation and desalination, to devices for energy storage and conversion, including fuel cells and batteries. In the discovery of new functional materials, synthetic chemistry plays a significant role whether being out of curiosity or guided by design principles.[48] Apart from the synthesis of membrane materials with entirely new molecular structures, the demonstrated approach of using physical blending of two miscible polymers proves effective, inexpensive, and straightforward to implement, generating a range of new membranes with great potential for electrochemical technologies from a synthetically accessible palette of polymers.

Supporting Information

Supporting Information is available from the Wiley Online Library or from the author.

Acknowledgements

Conflict of Interest

The authors declare no conflict of interest.

Author Contributions

Data Availability Statement

The data that support the findings of this study are available from the corresponding author upon reasonable request.

Keywords

[1] S. Bouckaert, A. F. Pales, C. McGlade, U. Remme, B. Wanner, L. Varro, D. D'Ambrosio, T. Spencer, *Net Zero by 2050: A Roadmap for the Global Energy Sector*, International Energy Agency, Paris, France **2021**.

[2] M. Park, J. Ryu, W. Wang, J. Cho, *Nat. Rev. Mater.* **2016**, 2, 16080.

[3] H. Zhang, W. Lu, X. Li, *Electrochem. Energy Rev.* **2019**, 2, 492.

[4] L. Zhang, R. Feng, W. Wang, G. Yu, *Nat. Rev. Chem.* **2022**, 6, 524.

[5] K. Lin, Q. Chen, M. R. Gerhardt, L. Tong, S. B. Kim, L. Eisenach, A. W. Valle, D. Hardee, R. G. Gordon, M. J. Aziz, M. P. Marshak, *Science* **2015**, 349, 1529.

[6] A. Hollas, X. Wei, V. Murugesan, Z. Nie, B. Li, D. Reed, J. Liu, V. Sprenkle, W. Wang, *Nat. Energy* **2018**, 3, 508.

[7] T. Liu, X. Wei, Z. Nie, V. Sprenkle, W. Wang, *Adv. Energy Mater.* **2016**, 6, 1501449.

[8] C. DeBruler, B. Hu, J. Moss, X. Liu, J. Luo, Y. Sun, T. L. Liu, *Chem* **2017**, 3, 961.

[9] R. Feng, X. Zhang, V. Murugesan, A. Hollas, Y. Chen, Y. Shao, E. Walter, N. P. N. Wellala, L. Yan, K. M. Rosso, W. Wang, *Science* **2021**, 372, 836.

[10] X. Li, P. Gao, Y.-Y. Lai, J. D. Bazak, A. Hollas, H.-Y. Lin, V. Murugesan, S. Zhang, C.-F. Cheng, W.-Y. Tung, *Nat. Energy* **2021**, 6, 873.

[11] M. Hu, A. Wang, T. Liu, J. Luo, **2022**, https://doi.org/10.26434/chemrxiv-2022-lqms7-v3.

[12] D. G. Kwabi, Y. Ji, M. J. Aziz, *Chem. Rev.* **2020**, 120, 6467.

[13] F. R. Brushett, M. J. Aziz, K. E. Rodby, *ACS Energy Lett.* **2020**, 5, 879.

[14] M. Wu, Y. Jing, A. A. Wong, E. M. Fell, S. Jin, Z. Tang, R. G. Gordon, M. J. Aziz, *Chem* **2020**, 6, 1432.

[15] Y. Ji, M. A. Goulet, D. A. Pollack, D. G. Kwabi, S. Jin, D. De Porcellinis, E. F. Kerr, R. G. Gordon, M. J. Aziz, *Adv. Energy Mater.* **2019**, *9*, 1900039.

[16] D. G. Kwabi, K. Lin, Y. Ji, E. F. Kerr, M.-A. Goulet, D. De Porcellinis, D. P. Tabor, D. A. Pollack, A. Aspuru-Guzik, R. G. Gordon, *Joule* **2018**, *2*, 1894.

[17] J. Friedl, M. A. Lebedeva, K. Porfyrakis, U. Stimming, T. W. Chamberlain, *J. Am. Chem. Soc.* **2018**, *140*, 401.

[18] J. Luo, B. Hu, C. Debruler, Y. Bi, Y. Zhao, B. Yuan, M. Hu, W. Wu, T. L. Liu, *Joule* **2019**, *3*, 149.

[19] A. Kusoglu, A. Z. Weber, *Chem. Rev.* **2017**, *117*, 987.

[20] D. W. Shin, M. D. Guiver, Y. M. Lee, *Chem. Rev.* **2017**, *117*, 4759.

[21] Q. Dai, Z. Zhao, M. Shi, C. Deng, H. Zhang, X. Li, *J. Membr. Sci.* **2021**, *632*, 119355.

[22] C. Li, S. M. Meckler, Z. P. Smith, J. E. Bachman, L. Maserati, J. R. Long, B. A. Helms, *Adv. Mater.* **2018**, *30*, 1704953.

[23] P. Zuo, Y. Li, A. Wang, R. Tan, Y. Liu, X. Liang, F. Sheng, G. Tang, L. Ge, L. Wu, Q. Song, N. B. McKeown, Z. Yang, T. Xu, *Angew. Chem., Int. Ed.* **2020**, *59*, 9564.

[24] J. Shen, G. Liu, Y. Han, W. Jin, *Nat. Rev. Mater.* **2021**, *6*, 294.

[25] M. J. Baran, M. E. Carrington, S. Sahu, A. Baskin, J. Song, M. A. Baird, K. S. Han, K. T. Mueller, S. J. Teat, S. M. Meckler, C. Fu, D. Prendergast, B. A. Helms, *Nature* **2021**, *592*, 225.

[26] R. Tan, A. Wang, R. Malpass-Evans, R. Williams, E. W. Zhao, T. Liu, C. Ye, X. Zhou, B. P. Darwich, Z. Fan, L. Turcani, E. Jackson, L. Chen, S. Y. Chong, T. Li, K. E. Jelfs, A. I. Cooper, N. P. Brandon, C. P. Grey, N. B. McKeown, Q. Song, *Nat. Mater.* **2020**, *19*, 195.

[27] M. J. Baran, M. N. Braten, S. Sahu, A. Baskin, S. M. Meckler, L. Li, L. Maserati, M. E. Carrington, Y.-M. Chiang, D. Prendergast, B. A. Helms, *Joule* **2019**, *3*, 2968.

[28] C. Ye, R. Tan, A. Wang, J. Chen, B. Comesaña Gándara, C. Breakwell, A. Alvarez-Fernandez, Z. Fan, J. Weng, C. G. Bezzu, S. Guldin, N. P. Brandon, A. R. Kucernak, K. E. Jelfs, N. B. McKeown, Q. Song, *Angew. Chem., Int. Ed.* **2022**, *61*, e202207580.

[29] J. E. Donald, D. W. Kulp, W. F. DeGrado, *Proteins: Struct., Funct., Bioinf.* **2011**, *79*, 898.

[30] H. R. Bosshard, D. N. Marti, I. Jelesarov, *J. Mol. Recognit.* **2004**, *17*, 1.

[31] X. Huang, X. Wang, M. Quan, H. Yao, H. Ke, W. Jiang, *Angew. Chem., Int. Ed.* **2021**, *60*, 1929.

[32] C. Van Stappen, Y. Deng, Y. Liu, H. Heidari, J.-X. Wang, Y. Zhou, A. P. Ledray, Y. Lu, *Chem. Rev.* **2022**, *122*, 11974.

[33] W. F. Yong, T.-S. Chung, *Polymer* **2015**, *59*, 290.

[34] W. F. Yong, F. Y. Li, T. S. Chung, Y. W. Tong, *J. Membr. Sci.* **2014**, *462*, 119.

[35] G.-H. Kim, D. Lee, A. Shanker, L. Shao, M. S. Kwon, D. Gidley, J. Kim, K. P. Pipe, *Nat. Mater.* **2015**, *14*, 295.

[36] J. J. Richardson, M. Björnmalm, F. Caruso, *Science* **2015**, *348*, aaa2491.

[37] Y. Xia, Y. Wang, H. Cao, S. Lin, Y. Xia, X. Hou, Y. Wu, Y. Yu, K. Huang, W. Xing, Z. Xu, *J. Membr. Sci.* **2022**, *653*, 120517.

[38] R. Yeo, C. H. Cheng, *J. Appl. Polym. Sci.* **1986**, *32*, 5733.

[39] K. Mizrahi Rodriguez, A. X. Wu, Q. Qian, G. Han, S. Lin, F. M. Benedetti, H. Lee, W. S. Chi, C. M. Doherty, Z. P. Smith, *Macromolecules* **2020**, *53*, 6220.

[40] C. Ye, A. Wang, C. Breakwell, R. Tan, C. G. Bezzu, E. Hunter-Sellars, D. R. Williams, N. P. Brandon, P. A. A. Klusener, A. R. Kucernak, K. E. Jelfs, N. B. McKeown, Q. Song, *Nat. Commun.* **2022**, *13*, 3184.

[41] J. W. Jeon, D.-G. Kim, E.-h. Sohn, Y. Yoo, Y. S. Kim, B. G. Kim, J.-C. Lee, *Macromolecules* **2017**, *50*, 8019.

[42] B. Santoso, P. Yanaranop, H. Kang, I. K. H. Leung, J. Jin, *Macromolecules* **2017**, *50*, 3043.

[43] B. Satilmis, P. M. Budd, *RSC Adv.* **2014**, *4*, 52189.

[44] J. M. J. Fréchet, *Science* **1994**, *263*, 1710.

[45] N. M. Luscombe, R. A. Laskowski, J. M. Thornton, *Nucleic Acids Res.* **2001**, *29*, 2860.

[46] J. Luo, A. Sam, B. Hu, C. DeBruler, X. Wei, W. Wang, T. L. Liu, *Nano Energy* **2017**, *42*, 215.

[47] E. Fell, D. De Porcellinis, Y. Jing, V. Gutierrez-Venegas, R. Gordon, S. Granados-Focil, M. Aziz, **2022**, https://doi.org/10.26434/chemrxiv-2022-zl7l6.

[48] A. K. Cheetham, R. Seshadri, F. Wudl, *Nat. Synth.* **2022**, *1*, 514.

2210098 (12 of 12)